

The first low-mass eclipsing binary within the fully convective zone from TMTS

Cheng Liu,^{1*} Xiaofeng Wang,^{2,1†} Xiaobing Zhang,³ Mikhail Kovalev,⁴ Jie Lin,^{2,5} Gaobo Xi,² Jun Mo,² Gaici Li,² Haowei Peng,² Xin Li,¹ Qiqi Xia,² Abdusamatjan Iskandar,⁶ Xiangyun Zeng,⁷ Letian Wang,⁶ Liying Zhu,⁴ Xuan Song,¹ Jincheng Guo,¹ Xiaojun Jiang,³ Shengyu Yan,² Jicheng Zhang⁸

¹Department of Scientific Research, Beijing Planetarium, Beijing 100044, China

²Physics Department and Tsinghua Center for Astrophysics, Tsinghua University, Beijing 100084, China

³CAS Key Laboratory of Optical Astronomy, National Astronomical Observatories, Chinese Academy of Sciences, Beijing 100101, China

⁴Yunnan Observatories, China Academy of Sciences, 650216 Kunming, China

⁵School of Astronomy and Space Sciences, University of Science and Technology of China, Hefei, 230026, China

⁶Xinjiang Astronomical Observatory, Chinese Academy of Sciences, Urumqi, Xinjiang 830011, People's Republic of China

⁷Center for Astronomy and Space Sciences, China Three Gorges University, Yichang 443000, China

⁸Department of Astronomy, Beijing Normal University, Beijing, 100875, China

Accepted 2024 May 3; Received 2024 April 24; in original form 2023 October 31

ABSTRACT

We present a comprehensive photometric and spectroscopic analysis of the short-period (~ 5.32 hours) and low-mass eclipsing binary TMTSJ0803 discovered by Tsinghua-Ma Huateng Telescope for Survey (TMTS). By fitting the light curves and radial velocity data with the Wilson–Devinney code, we find that the binary is composed of two late spotted active M dwarfs below the fully convective boundary. This is supported by the discovery of a significant Balmer emission lines in the LAMOST spectrum and prominent coronal X-ray emission. In comparison with the typical luminosity of rapidly rotating fully convective stars, the much brighter X-ray luminosity ($L_X/L_{\text{bol}} = 0.0159 \pm 0.0059$) suggests the stellar magnetic activity of fully convective stars could be enhanced in such a close binary system. Given the metallicity of $[M/H] = -0.35$ dex as inferred from the LAMOST spectrum, we measure the masses and radii of both stars to be $M_1 = 0.169 \pm 0.010 M_\odot$, $M_2 = 0.162 \pm 0.016 M_\odot$, $R_1 = 0.170 \pm 0.006 R_\odot$, and $R_2 = 0.156 \pm 0.006 R_\odot$, respectively. Based on the luminosity ratio from the light curve modeling, the effective temperatures of two components are also estimated. In comparison with the stellar evolution models, the radii and effective temperatures of two components are all below the isochrones. The radius deflation might be mainly biased by a small radial velocity (RV) data or (and) a simple correction on RVs, while the discrepancy in effective temperature might be due to the enhanced magnetic activity in this binary.

Key words: binaries: eclipsing – binaries: spectroscopic – stars: low-mass – stars: individual: TMTSJ0803

1 INTRODUCTION

Low-mass stars are the most common stellar objects in our galaxy (Henry et al. 2006; Feiden & Chaboyer 2012) and understanding them is thus clearly an important endeavour. Henry et al. (2006) found that at least $\sim 70\%$ of stars within 10 pc of the Sun are M dwarfs with $M \leq 0.6 M_\odot$. Such low-mass stars are useful probes of their structures (e.g. Jurić et al. 2008), kinematics (e.g. Bochanski et al. 2007), and chemical evolution (e.g. Woolf & West 2012; Souto et al. 2022). The fundamental properties of M dwarfs have become an essential component to studies of the initial mass function (e.g. Li et al. 2023). M dwarfs are also attractive targets for the identification and characterization of exoplanets. Due to smaller sizes, it is easier to find Earth-size planets around M dwarfs compared to FGK stars (e.g. Nutzman & Charbonneau 2008; Charbonneau et al. 2009).

In comparison with solar-type stars, stellar theory is not well understood for low-mass stars, especially in the regime of $0.08\text{--}0.3 M_\odot$, because of complex and varied physics inside the stars and active magnetic phenomena on their surfaces (Mullan & MacDonald 2001). The measurements of fundamental properties (mass, radius and effective temperature) are crucial for calibrating stellar evolution models. Careful observations of detached double-lined eclipsing binaries can result in model-independent mass and radius estimates to a precision better than 1% in some cases (e.g. Morales et al. 2009; Kraus et al. 2011). The first precise determinations of the fundamental parameters, obtained by Torres & Ribas (2002) and Ribas (2003) for early and mid-M dwarfs in two eclipsing systems YY Gem and CU Cnc, respectively, indicated that their radii are inflated by up to 20% with respect to the model predictions. The discrepancies between the observed radii of CM Dra and that predicted by stellar models were also noticed (e.g. Morales et al. 2009; Terrien et al. 2012), however, CM Dra is only inflated by about 2% compared to the prediction based on an older stellar age and a near-solar metallicity (Feiden &

* E-mail: liucheng@bjp.org.cn (CL)

† E-mail: wang_xf@tsinghua.edu.cn (XW)

Chaboyer 2014a). The M dwarfs with $M \gtrsim 0.35 M_{\odot}$ with inflated radii is well established by observations (Kraus et al. 2011; Spada et al. 2013; Cruz et al. 2018). In the range $M \lesssim 0.35 M_{\odot}$, however, the mass and radius of fewer stars can be accurately determined due to low brightness of cool and small objects (Zhou et al. 2014; Dittmann et al. 2017).

Recent studies suggested that most of the late M dwarfs in the fully convection regime follow the theoretical mass–radius relation (Hartman et al. 2018; von Boetticher et al. 2019; Maxted et al. 2022). Nevertheless, the effective temperatures measured for some low-mass cool stars were reported to be lower than those predicted by models (López-Morales & Ribas 2005; Morales et al. 2009; Zhou et al. 2015; Hartman et al. 2018). The study on white-dwarf and M dwarf binaries by Parsons et al. (2018) indicates that there is a 5% systematic bias towards larger radii for a sample of fully and partially convective low-mass stars, while the temperature measurements for the fully convection stars are in agreement with the theoretical predictions. The possible different trends of temperatures and radii between fully and partially convective stars may be caused by important transitions in inner structures of these stars (Chabrier & Baraffe 1997). This could be the explanation of a discontinuity in the effective temperature–radius relation discovered by Rabus et al. (2019) for M dwarfs.

It remains unclear whether the radius and temperature discrepancy is attributed to interior structure of low-mass stars or a systematic effect specific to the short-period binary systems. Stellar magnetic activity is a popular explanation of the inflation of radii of low-mass stars (Mullan & MacDonald 2001; Chabrier et al. 2007; Feiden & Chaboyer 2014b). The activity hypothesis is favored by observations of the short period binary systems (Morales et al. 2009; Kraus et al. 2011; Spada et al. 2013). The tidal interaction in such systems can give rise to a fast rotation of the companions, which is expected to generate strong magnetic fields and lead to larger stellar radii. The magnetic field might explain the radius inflation for M dwarfs with larger mass, however, its strength is unlikely stable in the fully convective interior of these stars (Feiden & Chaboyer 2014b). Other possible mechanisms include metallicity effects (Berger et al. 2006; von Boetticher et al. 2019) and magnetic star-spots on stars (e.g. Morales et al. 2010). A final solution to the discrepancies may be a combination of the above factors which likely all contribute to the interior structure of fully convective stars (Feiden & Chaboyer 2014a).

In order to probe different effects individually and in aggregate, more sample of low-mass eclipsing binary systems are needed. In this paper we report the study of a short-period eclipsing binary TMTS J08032285+3930509 (dubbed as TMTSJ0803) discovered during the TMTS survey (Lin et al. 2022), which consists of two detached M dwarfs in the fully convective mass range. As M dwarf system is very useful for testing theoretical models of low-mass stars, we utilize multicolor photometry from different telescopes and radial velocity (RV) measurements to constrain the masses and radii of both components of this binary system.

The paper is structured as follows. In Section 2, we describe the discovery, the follow-up photometric observations, and collection of the spectra. The light curve and period of the binary system is examined in Section 3. In Section 4, we estimate the properties of the binary via SED fitting and analysis of the LAMOST spectrum. In section 5, we calculate the absolute physical parameters of TMTJ0803 by a joint analysis of the light curves and RV data. In Section 6, we discuss the implications of these parameters in regards to the existing theoretical stellar models. We summarize in Section 7.

2 OBSERVATIONS

2.1 Photometric data from TMTS, SNOVA, TESS and TNT

TMTS is a photometric survey with four 40-cm optical telescopes located at Xinglong Observatory in China. The survey operates in such an observation mode: uninterrupted observing of the LAMOST areas for the whole night with a cadence of about 1 min, resulting in discoveries of many interesting short-period variables and eclipsing binaries (see more details in Zhang et al. 2020; Lin et al. 2022, 2023, 2024; Guo et al. 2024). A primary eclipse of TMTSJ0803 was observed on 2020 Jan. 15 in the first year TMTS survey (see Table 1). The system TMTSJ0803, alternative names are LP 208-19 and 2MASS J08032307+3930558, were first identified as an eclipsing binary by Palaversa et al. (2013). Based on the LAMOST spectrum and the continuous light curve observed on a whole night, we believe that TMTSJ0803 is a double M dwarfs binary system with a short period (~ 5.32 hours). TMTSJ0803 is the one of the first 12 short period double M dwarfs binary candidates selected from the database of TMTS survey, based on their light curves, (B-R) colors, and photometric and/or spectroscopic temperatures.

Follow-up photometric observations of TMTSJ0803 have been taken by SNOVA and Tsinghua-NAOC 0.8-m telescope (TNT; Wang et al. 2008; Huang et al. 2012). The SNOVA is a 36 cm telescope located at Nanshan Observatory in China, and it is used to monitor TMTSJ0803 in white light (clear band) and standard I band for a total of 8 nights, as shown in Table 1. TMTSJ0803 was also monitored in standard R band on 5 nights with the TNT at the Xinglong Observatory in December 2022. To achieve better photometry, we adopted different exposure time, ranging from 60s to 180s, for different telescopes and under different seeing conditions.

The standard image processing, such as bias correction, flat correction and source extraction are performed with Ccdproc of Astropy (Craig et al. 2017) and SExtractor (Bertin & Arnouts 1996). Four comparison stars are used to calibrate the photometry of TMTSJ0803.

In addition, TMTSJ0803 has also been observed by TESS (Ricker et al. 2015) in 3 sectors (20, 47, and 60) with cadences from 30 minutes to 200 seconds (see Table 1). For the long cadence observations in the Kepler mission, it was demonstrated by Zola et al. (2017) that the shapes of light curves of short-period (< 1.5 days) eclipsing binaries are influenced by the smearing effect. As the binary has a very short period, long exposure time in TESS observations would cause a significant influence on the shape of light curve of the binary. Therefore, the light curve from sector 60, at a cadence of 200 s, is only used to measure the physical parameters of the binary in Section 5.

2.2 Spectroscopic data from LAMOST

An optical spectrum of TMTSJ0803 was observed on 26th December 2014 by LAMOST (Cui et al. 2012) in low resolution mode ($R \sim 1800$; wavelength range 370 – 900 nm; Luo et al. 2015). This LAMOST spectrum has a bad quality in the blue arm due to the faintness of two these late M dwarfs at the blue end. While the average signal-to-noise (SNR) ratio of the spectrum is ~ 66 in the red end. The H_{α} emission can be clearly seen in Figure 3, where this emission feature observed at an orbital phase of about 0.48 was identified. The presence of prominent H_{α} emission line indicates that TMTSJ0803 could be very active (see more discussions in Sect. 6.1).

Based on the LAMOST spectrum, the atmospheric parameters of

Table 1. Observation logs of TMTSJ0803.

Telescope	Instrument	Obs_Date	Exposure (Bands)		
TMTS	CMOS	2020-01-15	60 s (Luminous filter)		
SNOVA	CCD	2021-01-18	60 s (C)		
		2021-02-28	120 s (C)		
		2021-10-17	90 s (C)		
		2022-01-11	90 s (I)		
		2022-01-13	90 s (I)		
		2022-12-16	90 s (C)		
		2022-12-21	90 s (C)		
		2022-12-24	180 s (I)		
		TNT	CCD	2022-12-27	60 s (R)
				2022-12-28	90 s (R)
2022-12-29	70 s (R)				
2022-12-30	70 s (R)				
2022-12-31	70 s (R)				
TESS	CCD	2019/Sector 20	1800 s		
		2021/Sector 47	600 s		
		2022/Sector 60	200 s		
LAMOST	Spectrograph	2014-12-25	5400 s		
APOGEE	Spectrograph	2012-12-02	1502x2 s		
		2013-03-30	2002x2 s		
		2016-10-29	2236x2 s		
		2016-10-30	3131x2 s		
		2016-12-05	4025x2 s		
		2016-12-06	4249x2 s		
		2017-02-01	4025x2 s		

C represents the white light without filter in the telescope.

TMTSJ0803 were provided in LAMOST DR7¹ as, effective temperature $T_{\text{eff}} = 3003 \pm 156$ K, surface gravity $\log g = 5.5 \pm 0.39$, metallicity $[M/H] = -0.62 \pm 0.52$ dex. However, we reexamine the atmospheric parameters of TMTSJ0803 using our own methodology in Sect. 4.2.

2.3 Spectroscopic data from APOGEE

TMTSJ0803 was also observed by the APOGEE (Apache Point Observatory Galactic Evolution Experiment) project in high-resolution mode, involving the APOGEE-N (north) spectrograph (Wilson et al. 2019) which cover a spectral range of $1.51\text{--}1.7 \mu\text{m}$ with an average resolution of $R \sim 22,500$ (Wilson et al. 2010, 2019). A total of seven infrared spectra can be extracted from the APOGEE DR16 database (Ahumada et al. 2020; Jönsson et al. 2020). Among them, four spectra were observed in 2016, while other three spectra were taken in 2012, 2013 and 2017, respectively, as listed in Table 1. The multiple-epoch spectra enable the measurements of RVs for individual components of TMTSJ0803 (see Table 2).

As the APOGEE DR16 pipeline constructed cross-correlation function (CCF) for each infrared spectrum, thus an automated code called apogeesb2² can be used to measure RV for each component by deconvolving the custom CCF (Kounkel et al. 2021). To identify the primary and secondary components, the apogeesb2 analyzes each CCF by utilizing the autonomous Gaussian deconvolution Python routine, GaussPy (Lindner et al. 2015). In this work, the $\log \alpha$ parameter is set to 3.1 to 3.8, depending on different spectrum rather than the recommended value 1.5 given in Kounkel et al. (2021). This is due to the relatively low quality of CCFs resulting from the low SNR of the APOGEE spectra.

¹ <http://dr7.lamost.org/v1.2/search>

² <https://github.com/mkounkel/apogeesb2>

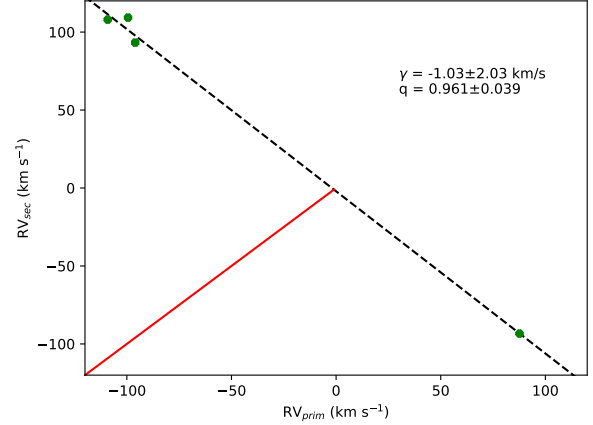


Figure 1. The Wilson plot. Green dots show velocities of the primary relative to those of the secondary. Black dash line shows the best fit to the data; the slope of this line relates to the mass ratio. Red line is the line of equality between RV_{prim} and RV_{sec} ; the intersection of these two lines corresponds to the barycentric velocity of the system.

The exposure time of each spectrum is usually longer than an hour except for the earliest spectrum observed in 2012. As mentioned in Section 2.1, the phase smearing effect caused by long exposure time can not be ignored. To evaluate the smearing effect on RV, we simply assume an identical sine curve for both primary and secondary stars because they have almost the same stellar mass as discussed in Section 6. Comparing the mean RV within the total exposure time with the one at the middle time, we then obtain the corrected RV value as listed in Table 2.

Although there is an insufficient number of epochs to construct a full orbital velocity variation, current measurements allow us to determine the mass ratio ($q = M_2/M_1$) and the central velocity (γ) for this binary by constructing a Wilson plot (Wilson 1941). We find that the mass ratio and the central velocity are $q = 0.961 \pm 0.039$ and $\gamma = -1.0 \pm 2.0 \text{ km s}^{-1}$, respectively. In Figure 1, the RV pairs from four epochs are used to measure q and γ . The first RV pair from epoch BJD 2456264.0093 is firstly removed because it is an outlier in the phased RV curves. We find that the absolute RVs ($> 57 \text{ km s}^{-1}$) at the first epoch are much higher than the expected values ($\sim 7 \text{ km s}^{-1}$) at phase 0.51. The contradiction might be caused by a wrong measurement of RVs at the first epoch. Two spectra observed at epoch BJD 2456381.7143 and 2457690.9798 are also abandoned, because the correction for phase smearing has a very large effect ($\Delta RV/RV_{1,2}^* > 100\%$) on their RVs and makes the RVs from these two spectra rather unreliable. Therefore, in Table 2 the first three RV pairs are ignored when the RV curves are used to constrain the semi-major axis (a) in Section 5.

3 PERIOD STUDY

To derive the orbital ephemeris of TMTSJ0803, we calculate the time of minimum light by fitting its light curve by a Gaussian function. A total of 389 minimum light epochs, 192 primary and 187 secondary ones, are obtained and listed in Table 3. With the least-square method, a linear ephemeris is derived by fitting the minimum light time as:

$$\begin{aligned} \text{Min.I} = & 2459579.765702 (\pm 0.000009) \\ & + 0.221871501 (\pm 0.00000007) \times E \end{aligned} \quad (1)$$

Table 2. Radial velocities from the APOGEE spectra.

BJD	RV ₁	RV ₁ [*]	σ ₁	RV ₂	RV ₂ [*]	σ ₂
–2450000 d	km s ^{–1}	km s ^{–1}	km s ^{–1}	km s ^{–1}	km s ^{–1}	km s ^{–1}
6264.0093	–52.55	–57.60	0.66	58.75	64.39	0.65
6381.7143	–38.04	–14.74	3.05	43.50	16.85	3.22
7690.9798	–64.05	–28.43	0.62	52.07	23.11	0.92
7691.9455	–77.19	–96.00	0.81	74.98	93.25	0.97
7727.8792	–75.17	–109.13	0.63	74.39	108.00	0.72
7728.8839	75.02	87.79	0.57	–79.91	–93.51	0.60
7785.7522	–72.40	–99.36	0.72	79.58	109.28	0.83

^{*} RV₁ stands for RV of the primary star, while RV₂ stands for that of the secondary star. Both RVs are corrected based on the exposure times.

Table 3. Minimum times of TMTSJ0803.

BJD	Error	Epoch	Filter
–2457000 d			
2233.20237	0.00001	–1562.0	SNOVA C
2233.31358	0.00001	–1561.5	SNOVA C
...
2591.08072	0.00027	51.0	SNOVA I
2591.19197	0.00050	51.5	SNOVA I
...
2579.87650	0.00036	0.5	TESS
2579.98671	0.00030	1.0	TESS
2580.09761	0.00033	1.5	TESS
2580.20884	0.00030	2.0	TESS
...
2944.30072	0.00016	1643.0	TNT R
2945.40989	0.00013	1648.0	TNT R
...
2962.38317	0.00025	1724.5	TESS
2962.49403	0.00020	1725.0	TESS

(This table is available in its entirety in machine-readable form.)

Figure 2 shows the linear fitting and the corresponding observed minus computed O – C residuals as a function of the epoch number E. It should be noted that the minimum-light time has a large error (more than 0.0007) and those values derived from eclipses without enough observation data are abandoned.

4 CHARACTERIZATION OF THE LOW-MASS ECLIPSING BINARY

4.1 Broad-band photometric characterization

A total of 19 broad-band photometric datapoints are available for TMTSJ0803, including GALEX_NUV (Bianchi et al. 2011), SDSS DR12 *u*, *g*, *r*, *i* (Alam et al. 2015), Pan-STARRS1 *g*, *r*, *i*, *z*, *y* (Chambers et al. 2016), Gaia DR2 *BP*, *G*, *RP* (Gaia Collaboration et al. 2018), 2MASS *J*, *H*, *K_s* (Skrutskie et al. 2006), WISE W1, W2 (Wright et al. 2010), and TESS (Ricker et al. 2015), which can be used to construct the spectral energy distribution (SED) with ARIADNE³ (spectral eneRgy distribution bAyesian moDel averagiNg fittEr, Vines & Jenkins 2022), constraining the effective temperature (T_{eff}), surface gravity ($\log g$), metallicity ($[M/H]$), distance (D) and V-band extinction of the binary system. With the Galactic reddening of $E(B-V)=0.045$ (Schlegel et al. 1998; Schlafly & Finkbeiner 2011) and adoption of extinction law from Fitzpatrick (1999), the best-fit parameters estimated for the system are: $T_{\text{eff}} = 2924 \pm 11$ K, $\log g$

$= 5.62 \pm 0.11$ dex, $[M/H] = -0.10 \pm 0.07$ dex, $D = 43.57 \pm 0.08$ pc, and $A_V = 0.07 \pm 0.01$ mag. These stellar parameters, except for metallicity, are consistent with the results from a single-star model presented in the next subsection. Here, the error on T_{eff} may be underestimated by the methodology. To estimate the possible systematic errors, we calculate the differences between the recommended values from literatures (see Table 3 in Vines & Jenkins 2022) and T_{eff} from the SED-fitting for 13 benchmark M dwarfs (< 3600 K) from Vines & Jenkins (2022), with no systematic offset being found (i.e., $\sim 1 \pm 180$ K).

4.2 Spectroscopic characterization by comparison with synthetic spectra

Using the full-spectrum fitting method developed by Kovalev et al. (2022), we analyze the LAMOST spectrum in binary and single-star spectral models (see details in Section 2.3 in Kovalev et al. 2022). For double M-type binary, the synthetic spectra from BT-Settl (AGSS2009) models (Allard et al. 2011, 2012) rather than the NLTE MPAI models are used in the analysis. Since there is no reliable absolute flux calibration for the LAMOST spectra, the observed spectrum is flux-renormalized by a fourth-order polynomial recommended from the loss function (Zhang et al. 2021). The synthetic spectrum of binary system is generated as a sum of two Doppler-shifted, normalized, and scaled single-star model spectra which are function of atmospheric parameters and stellar size. Comparing the synthetic binary spectrum with the observed one yields estimations of optimal T_{eff} , $\log g$, $[M/H]$, RV of each component, mass ratio q and one set of four coefficients of polynomials. On the other hand, the observed spectrum is also analysed with a single-star model, which is identical to a binary model when the parameters of both components are equal.

Owing to the quality of the spectrum in the blue end, only the spectrum of the red end ranging from 6800 Å to 8500 Å is fit by models, as shown in Figure 3. As the mass ratio q is measured from the RVs data discussed in Section 2.3, we fix $q = 0.96$ in order to find solution with minimal χ^2 in the spectral fitting program. Finally, we obtain the best atmospheric parameters in the single-star model: $T_{\text{eff}} = 2930$ K, $\log g = 5.33$ cgs, and $[M/H] = -0.35$ dex. For the binary model, we find $T_{\text{eff}} = 3000$ K, $\log g = 5.34$ cgs, and $[M/H] = -0.44$ dex for the primary star, and $T_{\text{eff}} = 2882$ K, $\log g = 5.27$ cgs, and $[M/H] = -0.44$ dex for the secondary star. The minimal χ^2 of these two fittings are shown in Figure 3. As the χ^2 from the binary model is larger than that of the single-star model, therefore, the atmospheric parameters from the single-star model would better constrain the binary properties by fitting to the light curves. Furthermore, by considering uncertainties, our estimated T_{eff} is consistent with the effective temperature of 3003 ± 156 K and 2974 ± 194 K measured from the LAMOST and APOGEE spectra, respectively. The effective temperatures of two components in the binary model are consistent with the results (see Table 4) derived from the light curve modeling (see Section 5).

Errors on T_{eff} , $\log g$ and $[M/H]$ are provided by the full-spectrum fitting method for both single-star and binary models. However, they are underestimated and nominal, such as $1 - 10$ K in T_{eff} , and 0.01 dex in $\log g$ and $[M/H]$, because the systematic errors are not included. Since the typical errors have been evaluated by Kovalev et al. (2022) using simulated datasets (see more details in their Sect. 2.3.3), we thus adopt the standard deviation of the test sample as our errors estimation. In this case, for the single-star model and primary component, the typical errors on T_{eff} , $\log g$ and $[M/H]$ is less than 150 K, 0.1 cgs, and 0.1 dex, respectively. For the secondary component,

³ <https://github.com/jvines/astroARIADNE>

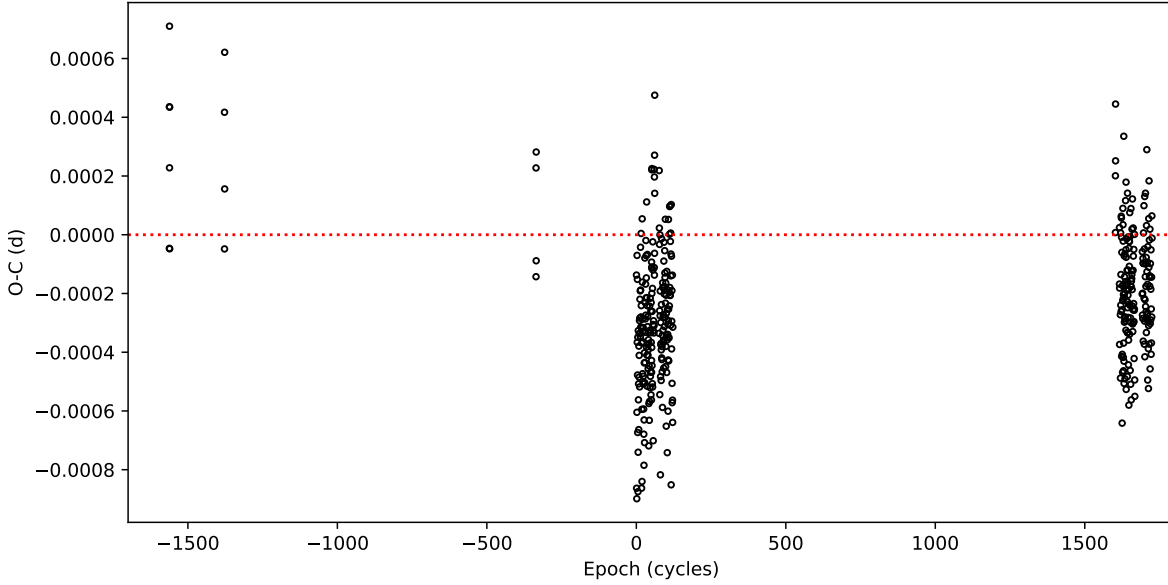


Figure 2. The corresponding O – C residuals after the linear fitting.

the typical errors on T_{eff} , $\log g$ and $[M/H]$ are less than 350 K, 0.2 cgs, and 0.2 dex, respectively.

5 BINARY MODELING

5.1 Modeling light curves and radial velocity shifts

To determine the properties of the binary, we use the 2015-version Wilson-Devinney (WD) code (Wilson & Devinney 1971; Wilson 1979, 1990, 2012; Wilson & Van Hamme 2014) to fit the light curves and the RVs simultaneously. In the subsequent analysis, the primary and the secondary stars are indicated with the subscripts 1 and 2, respectively. The small asymmetry (O’Connell effect (O’Connell 1951)) seen in the light curves, especially in the I band light curve shown in Figure 4, could be related to cool spots and/or hot spots on the surface of the stars. Since TMTSJ0803 is a detached system and the Balmer emission lines emerge in the LAMOST spectrum, we thus believe that the asymmetries in the light curves can be attributed to cool spots. Therefore, the binary model with spots (called Model B later) is applied to model the light curves. For comparison, another binary model without spot (called Model A) is also used to fit the light curves.

In the modelling, the effective temperature of the primary ($T_{\text{eff},1} = T_{\text{m}}$) is fixed to 2930 K according to the single-star spectral fitting result. According to the early studies by Lucy (1967) and Ruciński (1969), the gravity-darkening exponents $g_1 = g_2 = 0.32$ and the bolometric albedo $A_1 = A_2 = 0.5$ are adopted in the fitting, respectively. The bolometric and bandpass logarithmic limb-darkening coefficients are interpolated from the tables given in van Hamme (1993), Claret & Bloemen (2011) and Claret (2017). As the mass ratio (q) and the center-of-mass velocity (γ) were determined from the RV data, we therefore fix them in the binary modeling process. Moreover, the limited RV data can not provide enough constraint on the eccentricity (e), we thus simply assume it to be zero. During the fitting, the adjustable parameters are the semi-major axis of the binary (a), the

inclination (i), the effective temperature of the secondary ($T_{\text{eff},2}$), the surface potential (Ω_1 and Ω_2), the phase shift, the dimensionless luminosity of the primary (L_1), the spot parameters, longitude (ψ), spot angular radius (r), and temperature factor (T_s/T_*). Since the spot area and the latitude are highly correlated with temperature and radius of the star (Zhang et al. 2014), respectively, the latitude of the spot is assumed to be at 90° ($\theta \approx 1.571$ in radian).

It is well known that errors on the parameters provided by the WD code are underestimated. To overcome the drawback, firstly the observational errors⁴ are used as weights in our modeling processes to estimate the random errors. To estimate the systematic errors caused by the choices of input physics in the WD model, secondly numerous solutions are generated by choosing different gravity darkening exponents, limb darkening law and coefficients, albedo values, reflection effect, and whether or not to include spots. Here the systematic errors for i , $T_{\text{eff},2}$, Ω_1 , Ω_2 , a , and four equivalent radius (r) for each star are estimated and given in Table 4 (see the second error). We find that the systematic errors is at least twice times larger than the random errors, except for the errors of semi-major axis. Both the random and systematic errors are propagated to the uncertainties of the final absolute parameters, such as mass and radius. Although there is a small effect on some fitted parameter values caused by the spot, two WD models give us the same absolute parameters (see Table 4). This suggests that the free parameters are well constrained by the multiple light curves in this work.

5.2 Results

The best-fit light cures and RV curves (red solid lines) from the binary model and their corresponding O – C residuals are shown

⁴ Here the observational error is the standard deviation of the observational points in a small phase bin. The median errors in white light, I band, R band, and TESS data are 0.026, 0.018, 0.029, and 0.020 mag.

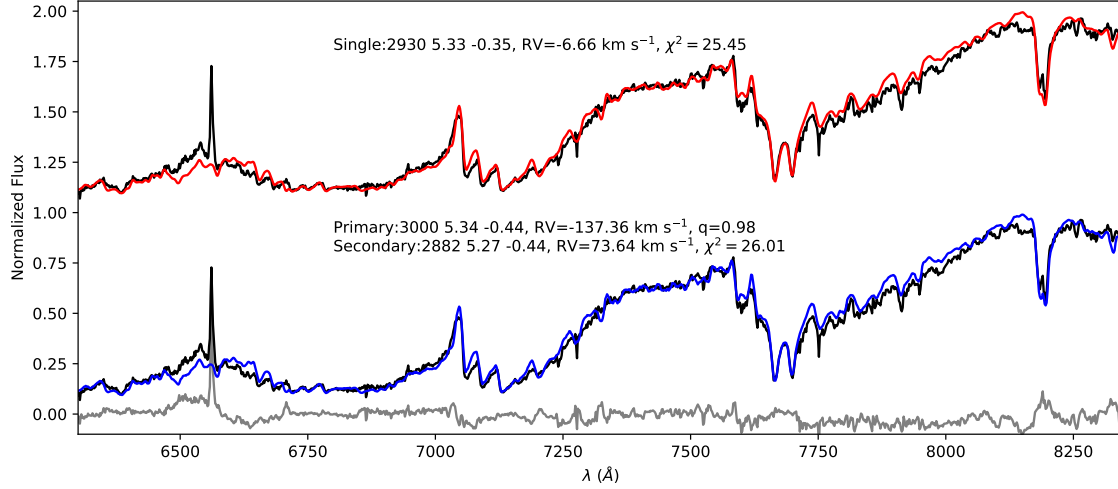


Figure 3. Comparison of the single-star (offset + 1.0) and binary model fits for TMTSJ0803. The difference of observed spectrum and single-star model spectrum is shown as gray line.

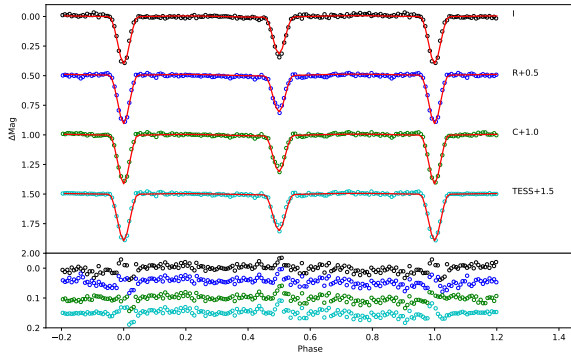


Figure 4. Upper panel: Light curves of TMTSJ0803. The points and solid lines represent the observed and theoretical light curves, respectively. Lower panel: residuals of the best-fit curves relative to the observed light curves.

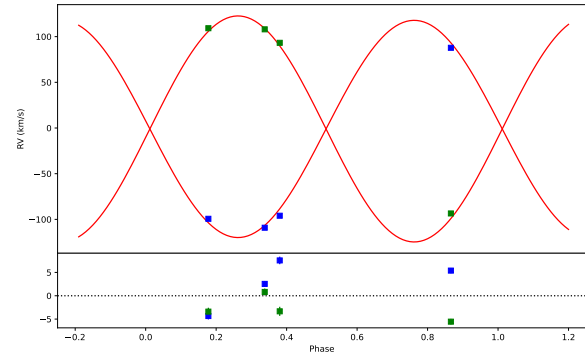


Figure 5. Upper panel: Differential radial velocity curves of the primary (blue squares) and secondary stars (green squares) of TMTSJ0803. The red lines represent corresponding fitting curves. Lower panel: residuals of the best-fit curves relative to the radial velocities.

in Figure 4 and 5, respectively. The results of the best-fit models are listed in Table 4, where the converge solutions without spot are listed in Model A and the solutions with one spot on the secondary are listed in Model B. The smaller value of $\sum(O - C)_i^2$ in Model B gives us a better solution. This is consistent with the conclusion in Sect. 6 that the binary system is active from the phenomenon of the Balmer emission lines, X-ray radiation and the flare events. Here, a third body around the binary system is tested, while the contribution of the third light to the total system is estimated to be almost zero in all bands.

Taking the semi-major axis of the binary (a) and the mass ratio (q) into the Kepler's third law ($M_1 + M_2 = 0.0134a^3/P^2$) and the equivalent radius ($r = R/a$), we calculate the mass and radius of primary and secondary star, respectively. The units of $M_{1,2}$, a , and P in the Kepler's equation should be M_\odot , R_\odot , and days, respectively. Although the uncertainties of the final absolute parameters are carefully estimated in the previous section, it is likely underestimated due to the limitation of RV data.

From Table 4, we find that the ratio of the temperature and luminosity between the secondary and the primary is determined to be ~ 0.96 and 1, respectively. As the low-resolution spectrum observed by LAMOST covers a phase range of 0.14 to 0.84, the light contribution from the secondary star to the observed spectrum can not be neglected. According to the study by Kjurkchieva et al. (2018), we then calculate the final temperatures:

$$T_{\text{eff},1} = T_m + \frac{c\Delta T}{c+1} \quad (2)$$

$$T_{\text{eff},2} = T_{\text{eff},1} - \Delta T \quad (3)$$

where $\Delta T = T_{\text{eff},1} - T_{\text{eff},2}$ and $c = L_2/L_1$ are calculated based on the final solutions from Model B. We find that the final $T_{\text{eff},1} = 2971 \text{ K}$ and $T_{\text{eff},2} = 2869 \text{ K}$ are consistent with the temperatures given by the binary spectral fitting method. Both the two empirical relations between effective temperature and spectral type, given by Bessell (1991) and Rajpurohit et al. (2013), suggest similar spectral types

Table 4. Light curve solution and physical parameters of the binary TMTSJ0803.

Parameter	Model A (no spot)	Model B (with spot) ^a
i (deg)	83.305±0.04	83.440±0.04±0.12
$T_{\text{eff},1}$ (K)	2930 (fixed) ^b	2930 (fixed) ^b
$T_{\text{eff},2}$ (K)	2836±2	2825±2±150
Ω_1	6.713±0.056	7.267±0.038±0.12
Ω_2	7.275±0.039	7.617±0.042±0.19
r_1 (pole)	0.158±0.001	0.158±0.001±0.003
r_1 (point)	0.160±0.001	0.160±0.001±0.003
r_1 (side)	0.159±0.001	0.159±0.001±0.003
r_1 (back)	0.160±0.001	0.160±0.001±0.003
r_2 (pole)	0.147±0.001	0.145±0.001±0.004
r_2 (point)	0.148±0.001	0.147±0.001±0.004
r_2 (side)	0.147±0.001	0.146±0.001±0.004
r_2 (back)	0.148±0.001	0.147±0.001±0.004
$L_1/(L_1 + L_2)(R)$	0.597±0.006	0.632±0.005
$L_1/(L_1 + L_2)(I)$	0.588±0.006	0.624±0.005
$L_1/(L_1 + L_2)(C)$	0.599±0.006	0.634±0.005
$L_1/(L_1 + L_2)(Tess)$	0.590±0.006	0.626±0.005
θ (rad)	—	1.571 (fixed) ^b
ψ (rad)	—	0.628±0.150
r (rad)	—	0.142±0.012
T_s/T_*	—	0.867±0.039
$\sum(O - C)_i^2$	0.065	0.058
Absolute parameters:		
a (R_\odot)	1.066±0.021	1.066±0.021±0.020
M_1 (M_\odot)	0.169±0.010	0.169±0.010
M_2 (M_\odot)	0.162±0.016	0.162±0.016
R_1 (R_\odot)	0.170±0.006	0.170±0.006
R_2 (R_\odot)	0.157±0.006	0.156±0.006
$\log g_1$ (cgs)	5.21±0.04	5.21±0.04
$\log g_2$ (cgs)	5.26±0.05	5.26±0.05
$\log L_1$ (L_\odot)	-2.695±0.006	-2.696±0.006
$\log L_2$ (L_\odot)	-2.830±0.006	-2.830±0.006

^a The systematic errors that are propagated to the uncertainties of the final absolute parameters are estimated for some parameters, such as, i , $T_{\text{eff},2}$, a and so on.

^b The primary temperature and spot latitude are fixed when modeling the light curves and spot on the star surface.

for primary (M5) and secondary star (M5.5). Therefore the detached binary system is composed of two similar late M dwarf (M5 + M5.5) stars.

6 DISCUSSIONS

6.1 Activity analysis

Chromospheric activity and star-spot activity could be triggered by magnetic fields and maintained by a magnetic dynamo. The spectral lines (H_α , H_β , H_γ , H_δ and Ca II H&K) are useful diagnostic indicators of chromospheric activity for late-type stars. The chromospheric activity of M stars shows emissions above continuum or core emissions in Balmer lines.

In our analysis, we first created a subtracted spectrum (the observed spectrum minus the synthetic spectrum from the binary model in Sect. 4.2) based on the observed LAMOST spectrum. When calculating the equivalent width of the H_α line (EW), we integrate the emission profile using the following formula

$$EW = \int_{\text{line}} \frac{F_\lambda - F_c}{F_c} d\lambda \quad (4)$$

where F_λ and F_c represent the fluxes of spectral line and the contin-

uum. Comparing the criteria (0.75 Å) for determining the chromospheric activity of M-type stars (West et al. 2011), the EW of H_α (2.63 Å) confirms the eclipsing binary is active.

The ratio of the H_α luminosity to the bolometric luminosity of the star, $L_{H_\alpha}/L_{\text{bol}}$, enables a better mass-independent comparison between activity levels in M dwarfs than EW alone (Newton et al. 2017). If we simply consider TMTSJ0803 as a single star, $L_{H_\alpha}/L_{\text{bol}}$ could be easily calculated: $L_{H_\alpha}/L_{\text{bol}} = EW \times \chi$ by adopting χ factor from Douglas et al. (2014). Our result ($L_{H_\alpha}/L_{\text{bol}} \sim 0.65 \pm 0.13 \times 10^{-4}$) is consistent with the values for most of rapidly rotating and full convective stars (Douglas et al. 2014; Newton et al. 2017).

Like the spectral lines, coronal X-ray emission is also a useful diagnostic of stellar activity. A close relation between the surface magnetic flux and X-ray radiance indicates that X-ray emission is a reliable proxy of magnetic activity (Wright & Drake 2016). Cross-matching with the updated ROSAT point-source catalogue (2RXS Boller et al. 2016) within 2 arcsecond, we find star ROSAT 2RXS J080322.0+393050 has a X-ray spectrum in the 0.1-2.4 keV energy band. With the SPIDERS program (Dwelly et al. 2017; Comparat et al. 2020), the observed instrumental ROSAT count rates can be converted into physical flux at $6.42965 \pm 2.40437 \times 10^{-13}$ mW/m². Given a parallax distance of 43.584 ± 0.10 pc (Bailer-Jones et al. 2021; Gaia Collaboration et al. 2021), the flux can be used to calculate the X-ray luminosity which is $L_X = 3.8175 \pm 1.4276 \times 10^{-5} L_\odot$. Combining with the Bolometric luminosity from the results of SED fitting in Section 4.1, we finally obtain $L_X/L_{\text{bol}} = 0.0159 \pm 0.0059$. Comparing with the fractional X-ray luminosity ($L_X/L_{\text{bol}} < 0.005$) of rapidly rotating fully convective stars, we find that the luminosity of TMTSJ0803 is 3 times brighter than that of the strongest X-ray stars in the catalog of Wright et al. (2011) and much higher than the mean saturation level of 10^{-3} . This suggests that stellar magnetic activity of fully convective stars could be significantly enhanced in a very close-by binary system such as TMTSJ0803. It is highly possible that the two components of this binary system have synchronized their rotation periods with the orbital period (i.e., ~ 5.32 hours) via tidal interaction. This is consistent with the discoveries that tidal locking leads to larger magnetic fields due to faster rotation rate (Spada et al. 2013; Gehan et al. 2022).

Flares are sudden and violent events that release magnetic energy and hot plasma from the stellar atmosphere. It is an indicator of the inherent activity of M dwarf stars. A clear flare event emerged around phase 0.23 on BJD 2459957.4416 was observed by TESS in sector 60. The flare duration was found to be ~ 50 min. Two more flares located around phase 0.69 and 0.83 were observed by TESS in sector 20 and 47, respectively. Those flares confirm that the system has stellar activity.

6.2 Comparisons with other M dwarf systems and stellar evolution models

Besides TMTSJ0803, there are 41 other M dwarf stars in eclipsing binaries with masses between 0.1 and $0.4 M_\odot$ and with masses and radii measured to have an accuracy better than 5%. Parameters of these binary systems are collected in Table 5. Figure 6, 7, and 8 show the mass–radius, mass– T_{eff} , and T_{eff} –radius relations for these objects, respectively. Inspecting the mass–radius and mass– T_{eff} plots reveals that the isochrones from the Dartmouth theoretical stellar evolution models show the best match with the observations. Although almost all the observed radii are above the age = 1 Gyr isochrone, they are consistent with the old and metal-rich isochrone ([Fe/H] = +0.5 dex, age = 10 Gyr) predicted by the Dartmouth models. This suggests that

most of the field stars may be old and/or metal-rich, while stars from open clusters (NGTS J0002-29A, B and PTFEB132.707+19.810A, B) are close to the young isochrone (age = 0.1 Gyr) in the mass–radius plot. Unlike the masses and radii are more consistent with the models, the observed effective temperatures are systematically lower than the models, especially the BHAC98 and BHAC15 models.

Figure 6 shows the locations of TMTSJ0803 in Radius–Mass relation as inferred from Models A and B, together with those of known sample of double M dwarf binaries (see also Table 4). Figure 7 shows distribution of TMTSJ0803 and the other sample in the T_{eff} –Mass relation. The outstanding feature is that the observed radii of two components of TMTSJ0803 are below the isochrones, while their effective temperatures are not outliers in the M dwarfs sample. Comparison with the stellar evolution models, smaller radii might be due to limited RV data or (and) a simple correction for RVs based only on the exposure times (see Section 2.3). We find from Table 2 that the difference between the original RV and corrected RV could be larger than 30 km s^{-1} . According to the third Kepler law, the semi-major axis is in proportion to the maximum RV of the binary when we fix the period. In this case, the uncorrected RV may decrease the radius by about 20% at least. Moreover, there is no RV data in the third quarter of the phase (see Figure 5). This might also cause bias in the final stellar radius. Therefore, it is not surprising that the radii of two components are slightly below the isochrones.

We find that different methodologies give different metallicities by fitting to the spectrum of TMTSJ0803. According to the parameters given by LAMOST DR7, the metallicity of this binary system is $[M/H] = -0.62$ dex with a large uncertainty. Comparing with the single-star model in Section 4.2, the binary model gives a $[M/H] = -0.44$ dex. From the combined infrared spectrum, we find that the best stellar atmospheric parameters have been provided by the pipeline ASPCAP in APOGEE DR14 (García Pérez et al. 2016; Abolfathi et al. 2018) and the system metallicity is $[M/H] = -0.94$ dex. Those suggest that the metallicity of TMTSJ0803 might be more poor than $[M/H] = -0.35$ dex used in this work. In this case, it would not be surprised that the estimated radii and temperatures are all below the isochrones.

Unlike a sharp transition identified by Rabus et al. (2019) for single M dwarfs, the M dwarfs in eclipsing binaries display a roughly linear feature between between stellar radius and T_{eff} , as seen in Figure 8. The above discrepancy can be explained by several reasons. Firstly, estimating the effective temperatures of a binary system is more challenging in comparison with single star, and the temperatures might suffer a larger bias and uncertainty, such as the system CU Cnc, LSPM J1112+7626, and MG1-2056316 listed in Table 5. Secondly, the data do not show a ‘discontinuity’ due to the lack of low-mass M dwarfs ($< 0.2 M_{\odot}$) with measurements of T_{eff} . Finally, there is a possibility that M dwarfs in different environments might have different characteristics. For instance, the stellar activity of individual components could be enhanced in close-binary as discussed in Section 6.1. The strong magnetic fields could inhibit convections in the atmosphere of stars (MacDonald & Mullan 2012).

7 CONCLUSIONS

We present a photometric and spectroscopic analysis of the short-period (~ 5.32 hours) eclipsing binary TMTSJ0803 detected by the TMTS. The analysis reveals that it is a late M dwarf binary whose components are below the fully convective boundary. Comparing with a normal eclipsing binary, the binary model (Model B) with one spot on the secondary provides the best fit to the light curves and RV

data. Under the assumption of the Kepler’s third law, we measure the masses and radii of both stars to be $M_1 = 0.169 \pm 0.010 M_{\odot}$, $M_2 = 0.162 \pm 0.016 M_{\odot}$, $R_1 = 0.170 \pm 0.006 R_{\odot}$, and $R_2 = 0.156 \pm 0.006 R_{\odot}$, respectively. Based on the luminosity ratio from the light curve modeling, the effective temperatures of two components of binary system are determined as $T_{\text{eff},1} = 2971 \text{ K}$ and $T_{\text{eff},2} = 2869 \text{ K}$, respectively. These are consistent with the results derived by fitting to the LAMOST spectrum with binary model.

The significant Balmer emission lines seen in the LAMOST spectrum of TMTSJ0803 suggest that this eclipsing binary is very active. Furthermore, we find that TMTSJ0803 has coronal X-ray emission and the fractional X-ray luminosity is $L_X/L_{\text{bol}} = 0.0159 \pm 0.0059$, which is much brighter than that of the typical rapidly rotating fully convective stars. This indicates that the stellar magnetic activity of the fully convective stars could be enhanced in close-by binary environment.

We find that both the radii and temperatures of the two components of TMTSJ0803 are below the isochrones. In comparison with the stellar evolution models, the radius deflation might be mainly biased by the limited RV data or (and) a simple correction for RVs. The effective temperature suppression might be due to enhanced magnetic activity in the binary. To better understand the origin of discrepancy in effective temperature and radius for this system, the higher-precision measurements of RV and photometric data are required. Combined with high-cadence photometric data, the LAMOST medium resolution survey gives us more opportunities to explore the nature of low-mass eclipsing binaries like TMTSJ0803 from TMTS.

ACKNOWLEDGEMENTS

This work is supported by the National Natural Science Foundation of China (NSFC NO. 12033003, 12288102, and 12203006), MaHuateng Foundation, and Beijing Natural Science Foundation (NO. 1242016). This work was partially supported by Science Program (BS202002), Talents Program (24CE-YS-08), the Innovation Project (23CB061 and 23CB059) and the Popular Science Project (24CD012) of Beijing Academy of Science and Technology, and the Tencent Xplorer Prize. LAMOST is funded by the National Development and Reform Commission and operated and managed by the National Astronomical Observatories, Chinese Academy of Sciences.

This work has made use of data from the publicly available SDSS data release. Funding for the Sloan Digital Sky Survey IV has been provided by the Alfred P. Sloan Foundation, the U.S. Department of Energy Office of Science, and the Participating Institutions. SDSS-IV acknowledges support and resources from the Center for High Performance Computing at the University of Utah. The SDSS website is www.sdss4.org.

SDSS-IV is managed by the Astrophysical Research Consortium for the Participating Institutions of the SDSS Collaboration including the Brazilian Participation Group, the Carnegie Institution for Science, Carnegie Mellon University, Center for Astrophysics | Harvard & Smithsonian, the Chilean Participation Group, the French Participation Group, Instituto de Astrofísica de Canarias, The Johns Hopkins University, Kavli Institute for the Physics and Mathematics of the Universe (IPMU) / University of Tokyo, the Korean Participation Group, Lawrence Berkeley National Laboratory, Leibniz Institut für Astrophysik Potsdam (AIP), Max-Planck-Institut für Astronomie (MPIA Heidelberg), Max-Planck-Institut für Astrophysik (MPA Garching), Max-Planck-Institut für Extraterrestrische Physik (MPE), National Astronomical Observatories of China, New Mexico

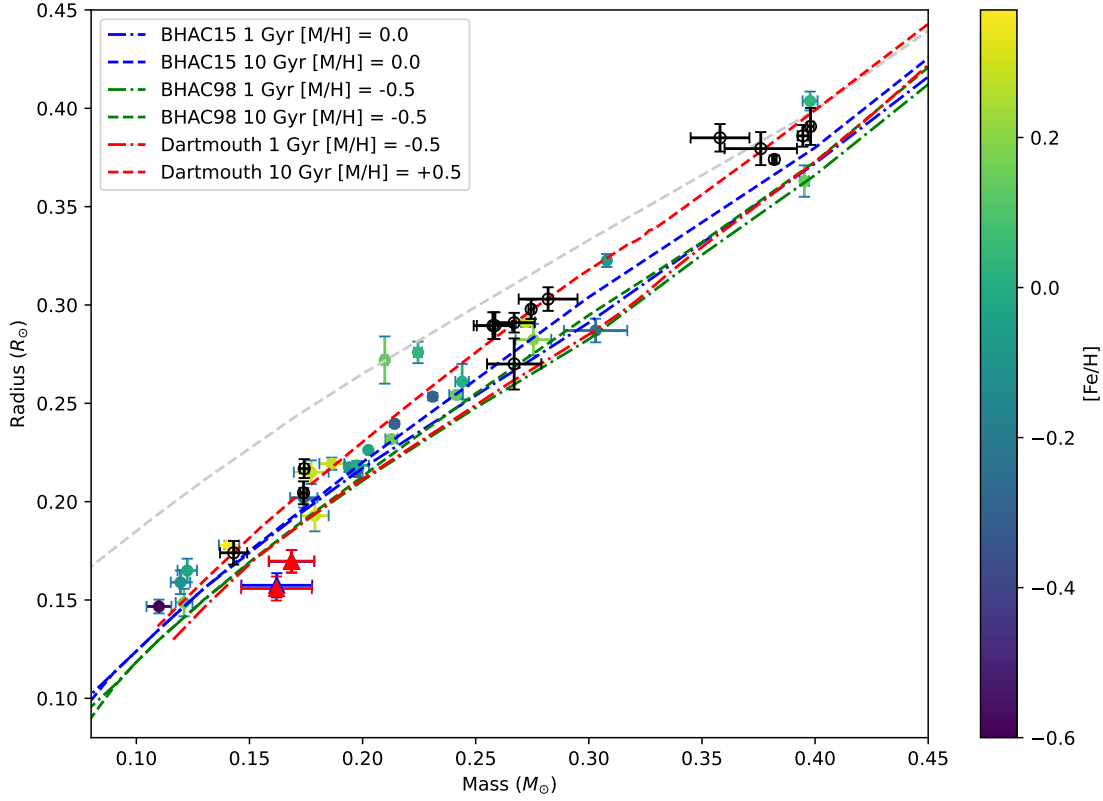


Figure 6. Mass–radius diagram for M dwarfs with $0.09 M_{\odot} < M < 0.40 M_{\odot}$. The color scale of the points indicates different metallicity. Large filled blue and red triangles show the components of TMTSJ0803 in Model A and B, respectively. Smaller circles show other M dwarfs with parameters given in Table 4. Black open circles are used for systems without a measured metallicity. The red dash and dot-dash lines show theoretical mass–radius relations from the Dartmouth (Dotter et al. 2008) models with different ages and metallicities. The blue and green lines represent the solar metallicity isochrones of BHAC15 (Baraffe et al. 2015), while the blue and green dash lines represent the sub-solar metallicity ($[\text{Fe}/\text{H}] = -0.5$ dex) isochrones of BHAC98 (Baraffe et al. 1998) age 1 and 10 Gyr.

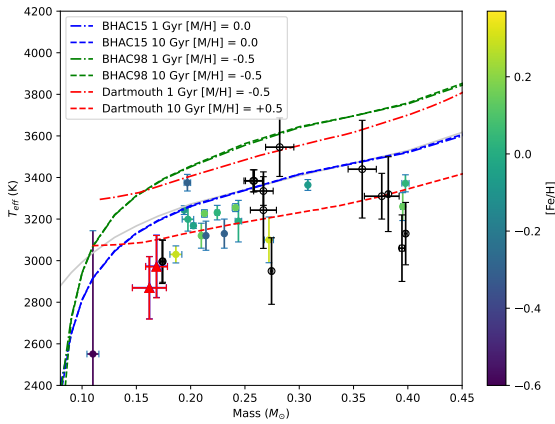


Figure 7. Similar to Figure 6, but we show the mass– T_{eff} diagram. The observed temperatures are systematically below the theoretical models, with even the 10 Gyr, $[\text{Fe}/\text{H}] = +0.5$ dex model being above about the half of the observations.

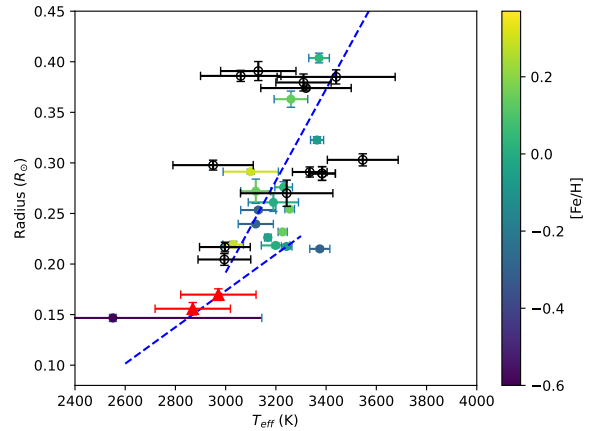


Figure 8. Similar to Figure 6, but here we show the T_{eff} –radius diagram. The dash blue lines represent the discontinuity of the T_{eff} –radius relation at stellar mass $0.23 M_{\odot}$ (Rabus et al. 2019). It looks like that there is no discontinuous behaviour for M dwarfs from binaries.

Table 5. The known M dwarfs in eclipsing binary systems with masses between 0.1 and 0.4 M_{\odot} , and with better determinations of masses and radii (i.e., < 5% error).

Star	Mass (M_{\odot})	Radius (R_{\odot})	T_{eff} (K)	[Fe/H] [*]	Reference(s)
CU Cnc B	0.3980±0.0014	0.3908±0.0094	3130±150	...	(Ribas 2003)
NGTS J0002-29A ^a	0.3978±0.0033	0.4037±0.0048	3372±41	+0.03±0.07	(Smith et al. 2021; Netopil et al. 2016)
PTFEB132.707+19.810A ^a	0.3953±0.0020	0.3630±0.0080	3260±67	+0.14±0.04	(Kraus et al. 2017)
LSPM J1112+7626A	0.3946±0.0023	0.3860±0.0055	3060±160	...	(Irwin et al. 2011)
MG1-2056316B	0.3820±0.0010	0.3740±0.0020	3320±180	...	(Kraus et al. 2011)
GJ 3236A	0.3760±0.0160	0.3795±0.0084	3310±110	...	(Irwin et al. 2009)
TYC 3576-2035-1	0.3580±0.0130	0.3850±0.0070	3440±235	...	(Jennings et al. 2023)
LP 661-13A ^b	0.30795±0.00084	0.3226±0.0033	...	-0.07±0.10	(Dittmann et al. 2017)
EBLM J1847+39B	0.3030±0.0140	0.2870±0.0060	...	-0.25±0.06	(Gill et al. 2019)
TYC 3121-1659-1	0.2820±0.0130	0.3030±0.0060	3546±141	...	(Jennings et al. 2023)
EBLM J1403-32B	0.2755±0.0079	0.2824±0.0080	...	+0.19±0.14	(von Boetticher et al. 2019)
LSPM J1112+7626B	0.2745±0.0012	0.2978±0.0049	2950±160	...	(Irwin et al. 2011)
HAT-TR-318-007B ^c	0.2721±0.0042	0.2913±0.0024	3100±110	+0.298±0.08	(Hartman et al. 2018)
TYC 3473-673-1	0.2670±0.0090	0.2910±0.0050	3335±69	...	(Jennings et al. 2023)
HAT-TR-205-003	0.2670±0.0120	0.2700±0.0130	3243±184	...	(Jennings et al. 2023)
IRXS J154727.5+450803B	0.2585±0.0080	0.2895±0.0068	(Hartman et al. 2011)
IRXS J154727.5+450803A	0.2576±0.0085	0.2895±0.0068	(Hartman et al. 2011)
HATS551-027A	0.2440±0.0030	0.2610±0.0090	3190±100	+0.00±0.20	(Zhou et al. 2015)
KOI-126B ^d	0.2413±0.0030	0.2543±0.0014	...	+0.15±0.08	(Carter et al. 2011)
CM Dra A ^c	0.2310±0.0009	0.2534±0.0019	3130±70	-0.30±0.12	(Morales et al. 2009; Terrien et al. 2012)
NGTS J0002-29B ^a	0.2245±0.0018	0.2759±0.0055	3231±35	+0.03±0.07	(Smith et al. 2021; Netopil et al. 2016)
CM Dra B ^c	0.2141±0.0010	0.2396±0.0015	3120±70	-0.30±0.12	(Morales et al. 2009; Terrien et al. 2012)
KOI-126C ^d	0.2127±0.0026	0.2318±0.0013	...	+0.15±0.08	(Carter et al. 2011)
PTFEB132.707+19.810B ^a	0.2098±0.0014	0.2720±0.0120	3120±60	+0.14±0.04	(Kraus et al. 2017)
Kepler-16B ^e	0.20255±0.00066	0.22623±0.00059	...	-0.30±0.20	(Doyle et al. 2011)
EBLM J2046+06B	0.1975±0.0053	0.2184±0.0023	3199±57	+0.00±0.05	(Swayne et al. 2021)
EBLM J0113+31B	0.1970±0.0030	0.2150±0.0020	3375±40	-0.30±0.10	(Maxted et al. 2022)
LP 661-13B ^b	0.19400±0.00034	0.2174±0.0023	...	-0.07±0.10	(Dittmann et al. 2017)
EBLM J1934-42B	0.1864±0.0055	0.2193±0.0031	3030±41	+0.29±0.05	(Swayne et al. 2021)
EBLM J1115-36B	0.1789±0.0061	0.1929±0.0080	...	+0.30±0.14	(von Boetticher et al. 2019)
EBLM J1013+01B	0.1773±0.0077	0.2150±0.0060	...	+0.29±0.14	(von Boetticher et al. 2019)
NGTS J0522-2507B	0.1742±0.0019	0.2168±0.0048	2997±101	...	(Casewell et al. 2018)
EBLM J2349-32B	0.1740±0.0060	0.2020±0.0050	...	-0.28±0.06	(Gill et al. 2019)
NGTS J0522-2507A	0.1739±0.0015	0.2045±0.0058	2995±105	...	(Casewell et al. 2018)
WTS 19g-4-02069B	0.1430±0.0060	0.1740±0.0060	(Nefs et al. 2013)
KIC 1571511B	0.1410±0.0045	0.1779±0.0020	...	+0.37±0.08	(Ofir et al. 2012)
TYC 2755-36-1	0.1390±0.0070	0.1720±0.0050	(Jennings et al. 2023)
GJ 65A	0.1225±0.0043	0.1650±0.0060	...	-0.03±0.20	(Kervella et al. 2016)
EBLM J1431-11B	0.1211±0.0037	0.1487±0.0070	...	+0.15±0.14	(von Boetticher et al. 2019)
GJ 65B	0.1195±0.0043	0.1590±0.0060	...	-0.12±0.20	(Kervella et al. 2016)
HATS550-016B	0.1100±0.0055	0.1467±0.0035	2551±593	-0.60±0.06	(Zhou et al. 2014; Jennings et al. 2023)

^{*} Normally, the listed metallicity is the value determined spectroscopically for the primary.

^a NGTS J0002-29 and PTFEB132.707+19.810 are the member of the Blanco 1 and Praesepe open cluster, respectively, and the adopted metallicity is the value for the cluster.

^b The metallicity of the LP 661-13 eclipsing binary system was not determined spectroscopically, but was estimated using the absolute K_s magnitude and the $M_{\text{Earth}}-K_s$ broadband color following Dittmann et al. (2016).

^c Assuming that both components have the same metallicity, the listed value is the binary system metallicities.

^d KOI-126B and KOI-126C are components of a triply eclipsing hierarchical triple system. The listed metallicity is the value determined spectroscopically for the primary.

^e The listed [Fe/H] is the [M/H] value determined spectroscopically for the primary.

State University, New York University, University of Notre Dame, Observatório Nacional / MCTI, The Ohio State University, Pennsylvania State University, Shanghai Astronomical Observatory, United Kingdom Participation Group, Universidad Nacional Autónoma de México, University of Arizona, University of Colorado Boulder, University of Oxford, University of Portsmouth, University of Utah, University of Virginia, University of Washington, University of Wisconsin, Vanderbilt University, and Yale University.

DATA AVAILABILITY

The minimum times of TMTSJ0803 are available in its online supplementary material. The TESS data presented in this paper were obtained from the Mikulski Archive for Space Telescopes (MAST) at the Space Telescope Science Institute (STScI) (<https://mast.stsci.edu>). Funding for the TESS mission is provided by the NASA Explorer Program directorate.

REFERENCES

- Abolfathi B., et al., 2018, *ApJS*, 235, 42
- Ahumada R., et al., 2020, *ApJS*, 249, 3
- Alam S., et al., 2015, *ApJS*, 219, 12
- Allard F., Homeier D., Freytag B., 2011, in Johns-Krull C., Browning M. K., West A. A., eds, *Astronomical Society of the Pacific Conference Series* Vol. 448, 16th Cambridge Workshop on Cool Stars, Stellar Systems, and the Sun. p. 91 ([arXiv:1011.5405](https://arxiv.org/abs/1011.5405))
- Allard F., Homeier D., Freytag B., 2012, *Philosophical Transactions of the Royal Society of London Series A*, 370, 2765
- Bailer-Jones C. A. L., Rybizki J., Foesneanu M., Demleitner M., Andrae R., 2021, *AJ*, 161, 147
- Baraffe I., Chabrier G., Allard F., Hauschildt P. H., 1998, *A&A*, 337, 403
- Baraffe I., Homeier D., Allard F., Chabrier G., 2015, *A&A*, 577, A42
- Berger D. H., et al., 2006, *ApJ*, 644, 475
- Bertin E., Arnouts S., 1996, *A&AS*, 117, 393
- Bessell M. S., 1991, *AJ*, 101, 662
- Bianchi L., Herald J., Efremova B., Girardi L., Zobot A., Marigo P., Conti A., Shiao B., 2011, *Ap&SS*, 335, 161
- Bochanski J. J., Munn J. A., Hawley S. L., West A. A., Covey K. R., Schneider D. P., 2007, *AJ*, 134, 2418
- Boller T., Freyberg M. J., Trümper J., Haberl F., Voges W., Nandra K., 2016, *A&A*, 588, A103
- Carter J. A., et al., 2011, *Science*, 331, 562
- Casewell S. L., et al., 2018, *MNRAS*, 481, 1897
- Chabrier G., Baraffe I., 1997, *A&A*, 327, 1039
- Chabrier G., Gallardo J., Baraffe I., 2007, *A&A*, 472, L17
- Chambers K. C., et al., 2016, *arXiv e-prints*, p. [arXiv:1612.05560](https://arxiv.org/abs/1612.05560)
- Charbonneau D., et al., 2009, *Nature*, 462, 891
- Claret A., 2017, *A&A*, 600, A30
- Claret A., Bloemen S., 2011, *A&A*, 529, A75
- Comparat J., et al., 2020, *A&A*, 636, A97
- Craig M., et al., 2017, *Astropy/Ccdproc: V1.3.0.Post1*, Zenodo, [doi:10.5281/zenodo.1069648](https://doi.org/10.5281/zenodo.1069648)
- Cruz P., Diaz M., Birkby J., Barrado D., Sipőcz B., Hodgkin S., 2018, *MNRAS*, 476, 5253
- Cui X.-Q., et al., 2012, *Research in Astronomy and Astrophysics*, 12, 1197
- Dittmann J. A., Irwin J. M., Charbonneau D., Newton E. R., 2016, *ApJ*, 818, 153
- Dittmann J. A., et al., 2017, *ApJ*, 836, 124
- Dotter A., Chaboyer B., Jevremović D., Kostov V., Baron E., Ferguson J. W., 2008, *ApJS*, 178, 89
- Douglas S. T., et al., 2014, *ApJ*, 795, 161
- Doyle L. R., et al., 2011, *Science*, 333, 1602
- Dwelly T., et al., 2017, *MNRAS*, 469, 1065
- Feiden G. A., Chaboyer B., 2012, *ApJ*, 757, 42
- Feiden G. A., Chaboyer B., 2014a, *A&A*, 571, A70
- Feiden G. A., Chaboyer B., 2014b, *ApJ*, 789, 53
- Fitzpatrick E. L., 1999, *PASP*, 111, 63
- Gaia Collaboration et al., 2018, *A&A*, 616, A1
- Gaia Collaboration et al., 2021, *A&A*, 649, A1
- García Pérez A. E., et al., 2016, *AJ*, 151, 144
- Gehan C., Gaulme P., Yu J., 2022, *A&A*, 668, A116
- Gill S., et al., 2019, *A&A*, 626, A119
- Guo F., et al., 2024, *MNRAS*, 528, 6997
- Hartman J. D., Bakos G. Á., Noyes R. W., Sipőcz B., Kovács G., Mazeh T., Shporer A., Pál A., 2011, *AJ*, 141, 166
- Hartman J. D., et al., 2018, *AJ*, 155, 114
- Henry T. J., Jao W.-C., Subasavage J. P., Beaulieu T. D., Ianna P. A., Costa E., Méndez R. A., 2006, *AJ*, 132, 2360
- Huang F., Li J.-Z., Wang X.-F., Shang R.-C., Zhang T.-M., Hu J.-Y., Qiu Y.-L., Jiang X.-J., 2012, *Research in Astronomy and Astrophysics*, 12, 1585
- Irwin J., et al., 2009, *ApJ*, 701, 1436
- Irwin J. M., et al., 2011, *ApJ*, 742, 123
- Jennings Z., Southworth J., Maxted P. F. L., Mancini L., 2023, *MNRAS*, 521, 3405
- Jönsson H., et al., 2020, *AJ*, 160, 120
- Jurić M., et al., 2008, *ApJ*, 673, 864
- Kervella P., Mérand A., Ledoux C., Demory B. O., Le Bouquin J. B., 2016, *A&A*, 593, A127
- Kjurkchieva D. P., Dimitrov D. P., Ibryamov S. I., Vasileva D. L., 2018, *Publ. Astron. Soc. Australia*, 35, e008
- Kounkel M., et al., 2021, *AJ*, 162, 184
- Kovalev M., Li Z., Zhang X., Li J., Chen X., Han Z., 2022, *MNRAS*, 513, 4295
- Kraus A. L., Tucker R. A., Thompson M. I., Craine E. R., Hillenbrand L. A., 2011, *ApJ*, 728, 48
- Kraus A. L., et al., 2017, *ApJ*, 845, 72
- Li J., Liu C., Zhang Z.-Y., Tian H., Fu X., Li J., Yan Z.-Q., 2023, *Nature*, 613, 460
- Lin J., et al., 2022, *MNRAS*, 509, 2362
- Lin J., et al., 2023, *MNRAS*, 523, 2172
- Lin J., et al., 2024, *Nature Astronomy*,
- Lindner R. R., et al., 2015, *AJ*, 149, 138
- López-Morales M., Ribas I., 2005, *ApJ*, 631, 1120
- Lucy L. B., 1967, *Z. Astrophys.*, 65, 89
- Luo A. L., et al., 2015, *Research in Astronomy and Astrophysics*, 15, 1095
- MacDonald J., Mullan D. J., 2012, *MNRAS*, 421, 3084
- Maxted P. F. L., et al., 2022, *MNRAS*, 513, 6042
- Morales J. C., et al., 2009, *ApJ*, 691, 1400
- Morales J. C., Gallardo J., Ribas I., Jordi C., Baraffe I., Chabrier G., 2010, *ApJ*, 718, 502
- Mullan D. J., MacDonald J., 2001, *ApJ*, 559, 353
- Nefs S. V., et al., 2013, *MNRAS*, 431, 3240
- Netopil M., Paunzen E., Heiter U., Soubiran C., 2016, *A&A*, 585, A150
- Newton E. R., Irwin J., Charbonneau D., Berlind P., Calkins M. L., Mink J., 2017, *ApJ*, 834, 85
- Nutzman P., Charbonneau D., 2008, *PASP*, 120, 317
- O'Connell D. J. K., 1951, *Publications of the Riverview College Observatory*, 2, 85
- Ofr A., Gandolfi D., Buchhave L., Lacy C. H. S., Hatzes A. P., Fridlund M., 2012, *MNRAS*, 423, L1
- Palaversa L., et al., 2013, *AJ*, 146, 101
- Parsons S. G., et al., 2018, *MNRAS*, 481, 1083
- Rabus M., et al., 2019, *MNRAS*, 484, 2674
- Rajpurohit A. S., Reylé C., Allard F., Homeier D., Schultheis M., Bessell M. S., Robin A. C., 2013, *A&A*, 556, A15
- Ribas I., 2003, *A&A*, 398, 239
- Ricker G. R., et al., 2015, *Journal of Astronomical Telescopes, Instruments, and Systems*, 1, 014003
- Ruciński S. M., 1969, *Acta Astron.*, 19, 245
- Schlafly E. F., Finkbeiner D. P., 2011, *ApJ*, 737, 103
- Schlegel D. J., Finkbeiner D. P., Davis M., 1998, *ApJ*, 500, 525
- Skrutskie M. F., et al., 2006, *AJ*, 131, 1163
- Smith G. D., et al., 2021, *MNRAS*, 507, 5991
- Souto D., et al., 2022, *ApJ*, 927, 123
- Spada F., Demarque P., Kim Y. C., Sills A., 2013, *ApJ*, 776, 87
- Swayne M. I., et al., 2021, *MNRAS*, 506, 306
- Terrien R. C., Fleming S. W., Mahadevan S., Deshpande R., Feiden G. A., Bender C. F., Ramsey L. W., 2012, *ApJ*, 760, L9
- Torres G., Ribas I., 2002, *ApJ*, 567, 1140
- Vines J. I., Jenkins J. S., 2022, *MNRAS*, 513, 2719
- Wang X., et al., 2008, *ApJ*, 675, 626
- West A. A., et al., 2011, *AJ*, 141, 97
- Wilson O. C., 1941, *ApJ*, 93, 29
- Wilson R. E., 1979, *ApJ*, 234, 1054
- Wilson R. E., 1990, *ApJ*, 356, 613
- Wilson R. E., 2012, *AJ*, 144, 73
- Wilson R. E., Devinney E. J., 1971, *ApJ*, 166, 605
- Wilson R. E., Van Hamme W., 2014, *ApJ*, 780, 151
- Wilson J. C., et al., 2010, in McLean I. S., Ramsay S. K., Takami H., eds, *Society of Photo-Optical Instrumentation Engineers (SPIE) Conference Series* Vol. 7735, *Ground-based and Airborne Instrumentation for Astronomy III*. p. 77351C, [doi:10.1117/12.856708](https://doi.org/10.1117/12.856708)

- Wilson J. C., et al., 2019, *PASP*, 131, 055001
Woolf V. M., West A. A., 2012, *MNRAS*, 422, 1489
Wright N. J., Drake J. J., 2016, *Nature*, 535, 526
Wright E. L., et al., 2010, *AJ*, 140, 1868
Wright N. J., Drake J. J., Mamajek E. E., Henry G. W., 2011, *ApJ*, 743, 48
Zhang L.-Y., Pi Q.-f., Yang Y.-G., 2014, *MNRAS*, 442, 2620
Zhang J.-C., et al., 2020, *PASP*, 132, 125001
Zhang S., et al., 2021, *ApJ*, 908, 131
Zhou G., et al., 2014, *MNRAS*, 437, 2831
Zhou G., et al., 2015, *MNRAS*, 451, 2263
Zola S., Baran A., Debski B., Jableka D., 2017, *MNRAS*, 466, 2488
van Hamme W., 1993, *AJ*, 106, 2096
von Boetticher A., et al., 2019, *A&A*, 625, A150

This paper has been typeset from a $\text{\TeX}/\text{\LaTeX}$ file prepared by the author.